

# Model-Based Quantitation of 3-D Magnetic Resonance Angiographic Images

Alejandro F. Frangi,\* *Student Member, IEEE*, Wiro J. Niessen, *Member, IEEE*,  
Romhild M. Hoogeveen, Theo van Walsum, and Max A. Viergever

**Abstract**—Quantification of the degree of stenosis or vessel dimensions are important for diagnosis of vascular diseases and planning vascular interventions. Although diagnosis from three-dimensional (3-D) magnetic resonance angiograms (MRA's) is mainly performed on two-dimensional (2-D) maximum intensity projections, automated quantification of vascular segments directly from the 3-D dataset is desirable to provide accurate and objective measurements of the 3-D anatomy.

A model-based method for quantitative 3-D MRA is proposed. Linear vessel segments are modeled with a central vessel axis curve coupled to a vessel wall surface. A novel image feature to guide the deformation of the central vessel axis is introduced. Subsequently, concepts of deformable models are combined with knowledge of the physics of the acquisition technique to accurately segment the vessel wall and compute the vessel diameter and other geometrical properties.

The method is illustrated and validated on a carotid bifurcation phantom, with ground truth and medical experts as comparisons. Also, results on 3-D time-of-flight (TOF) MRA images of the carotids are shown. The approach is a promising technique to assess several geometrical vascular parameters directly on the source 3-D images, providing an objective mechanism for stenosis grading.

**Index Terms**—Magnetic resonance angiography, model-based image analysis, quantification, stenosis grading.

## I. INTRODUCTION

ACCURATE determination of vessel width is important in grading vascular stenosis. Stenosis quantification in the carotid arteries, for instance, determines the choice of stroke treatment. Studies have revealed that a patient with a severe ( $>70\%$ ) symptomatic stenosis in the carotids should be operated on, while patients with stenoses smaller than  $30\%$  should not undergo surgical treatment [1], [2]. The benefit of surgery in cases of stenosis with severity between  $30$  and  $70\%$  is still under investigation [2], [3]. These findings support the relevance of accurate measurement techniques of vascular segments.

Magnetic resonance angiography (MRA) is a technique which can supply three-dimensional (3-D) information of the

vasculature. Although evaluation by radiologists is mainly performed on two-dimensional (2-D) maximum intensity projections (MIP's) [4], it is known that these lead to vessel width underestimation and a decreased contrast-to-noise ratio (CNR) [4]–[6].

In order to improve grading of stenoses it would be desirable to obtain quantitative morphological information directly from the original 3-D images, and not only from their projections [7]–[9]. To this end, accurate 3-D segmentation tools are required.

Vessel enhancement and segmentation of 3-D images has been investigated by many researchers. A number of approaches analyze the images at a single scale [10]–[16], which limits their applicability to images in which the range of vessel widths is small. This is probably the reason for the observation made in [10], [11], and [13] that small vessels are better enhanced than large vessels. A number of papers have acknowledged the importance of multiscale algorithms that can cope with vessel width variability [17]–[26].

The majority of approaches for vessel enhancement and segmentation [17]–[22], [25] rely on purely morphological criteria.<sup>1</sup> This has the advantage that the method is applicable to a wide variety of imaging modalities. However, the physics of the image formation influences the eventual depiction of the vessels and not taking this into account may lead to important structural measurement errors. Consider, for instance, the multiscale approaches that estimate vessel width on the basis of the scale of maximum response of some differential operators [17]–[25], as suggested in the seminal work on scale selection by Lindeberg [27]. In these approaches, a number of assumptions are made: the vessel is circular with radius equal to some empirical function of scale [17], [20]–[22], [24], [25]. This leads to the fact that the discretization of the scale parameter *a priori* determines the possible vessel diameters. This is specially problematic when one considers that the number of scales is in general small, to reduce the computational burden involved in multiscale methods. However, multiscale vessel enhancement methods have proven to be very useful for reconstructing the vessel tree, in order to provide a 3-D visualization. This can be highly valuable for surgical planning where the relative location of the vessels, rather than their precise width, is the important

Manuscript received March 19, 1999; revised September 17, 1999. This work was supported in part by the Dutch Ministry of Economic Affairs under Project IOP Beeldverwerking IBV97009. The Associate Editor responsible for coordinating the review of this paper and recommending its publication was D. Hawkes. Asterisk indicates corresponding author.

A. F. Frangi, W. J. Niessen, R. M. Hoogeveen, T. van Walsum, and M. A. Viergever are with the Image Sciences Institute (ISI), University Medical Center, Room E.01.334, Heidelberglaan 100, 3584 CX, Utrecht, The Netherlands.

Publisher Item Identifier S 0278-0062(99)09634-2.

<sup>1</sup>Summers *et al.* [26], however, used phase-contrast MR images and, therefore, could also incorporate flow directionality information. Note that in this paper our main concern is to obtain accurate vessel dimensions and not flow information.

issue. However, accurate quantification in these approaches is limited, since the underlying assumptions are often not valid, especially in pathological conditions [28], [29]. The fact that very few quantitative evaluation results have been reported in the literature reveals, to some extent, the difficulty of obtaining accurate measurements with purely geometry guided algorithms. To our knowledge, a few schemes have been proposed for automated quantitative angiography which focus on quantitative coronary angiography (QCA) [30], [31] from 2-D X-ray DSA images. Little work has been reported, however, on automated quantitative MRA directly from the 3-D data. So, whereas the area of vessel enhancement and segmentation has received considerable attention, there is still progress to be made in automated quantitative 3-D MRA.

In this paper we suggest a novel scheme for quantitative vessel analysis from MRA that uses knowledge of the image formation process to accurately define vessel boundaries. The procedure operates on the 3-D source images (not their projections), using a 3-D deformable model. The model consists of a representation of a central vessel axis coupled to a vessel wall surface. The use of a B-spline representation for the curve and surface models enables the use of already existing powerful interaction mechanisms inherited from computer-assisted design (CAD). For initialization, which is an important step in segmentation schemes based on deformable models, we introduce a technique based on an isosurface rendering of the vasculature, which allows for intuitive and efficient interaction in a 3-D setting.

The paper is organized as follows. In Section II we introduce a model-based approach to estimate the central axis and width of a vessel. Section III discusses some implementation details. Section IV describes the materials and methods involved in the validation of our algorithm with phantom experiments and clinical MRA datasets. After the results of the validation are presented in Section V, the paper is concluded with a discussion (Section VI).

## II. MODEL-BASED VESSEL SEGMENTATION

In this section, a two-step vessel segmentation procedure is proposed. First, a representation of the central vessel axis is obtained. This axis is subsequently used as a reference for extracting the boundaries of the vessel.

### A. Central Vessel Axis Model

The central vessel axis,  $\mathbf{C}(v)$  is modeled using a B-spline curve of degree  $n$  with  $s+1$  control points. This representation enforces the lumen line to be connected

$$\mathbf{C}(v) = \sum_{i=0}^s N_{in}(v) \mathbf{P}_i.$$

Here,  $\mathbf{P}_i$  are the control points,  $N_{in}(v)$  is the  $i$ -th B-spline basis function of order  $n$  [32], and  $v \in [0, 1]$ . The model (sometimes referred to as a *snake*) deforms toward the center of the vessel by minimizing an energy functional,  $\mathcal{E}^C$ , containing terms associated with the shape of the spline and the image contents [33], [34]

$$\mathcal{E}^C = \mathcal{E}_{\text{external}}^C + \gamma_s^C \mathcal{E}_{\text{stretching}}^C + \gamma_b^C \mathcal{E}_{\text{bending}}^C \quad (1)$$

where

$$\begin{aligned} \mathcal{E}_{\text{stretching}}^C &= \frac{1}{\ell} \int_0^1 \|\mathbf{C}_v(v)\|^2 \|\mathbf{C}_v(v)\| dv \\ \mathcal{E}_{\text{bending}}^C &= \frac{1}{\ell} \int_0^1 \|\mathbf{C}_{vv}(v)\|^2 \|\mathbf{C}_v(v)\| dv \\ \ell &= \int_0^1 \|\mathbf{C}_v(v)\| dv \end{aligned}$$

provide the internal constraints over the first- and second-order parametric derivatives. If we consider the central vessel axis as a physical string, these constraints are associated with simple approximations [35] to its stretch and bending energies, respectively. The constants  $\gamma_s^C$  and  $\gamma_b^C$  regulate the contribution of the internal forces with respect to that of the external (or image driven) force. In the physical analogy, the optimization process is interpreted as the evolution of the model toward a state of minimal energy.

The external energy is used to attract the curve toward points which have a high likelihood of lying along the central vessel axis. For this purpose, a new filter [18] has been developed that has the following properties: 1) it filters out non-line-like structures; 2) it is maximum at the center of the vessel; and 3) it is sensitive to vessels of different sizes.

The filter computes the eigenvalues and eigenvectors of the Hessian matrix at multiple scales  $\sigma$ . The eigenvalues are then combined into a discriminant function that has maximum response for structures behaving as a tube at scale  $\sigma$ .

We shall now formalize these ideas. Let  $\mathcal{H}_\sigma$  be the Hessian matrix at a given voxel  $\mathbf{x}$

$$\mathcal{H}_\sigma = \begin{bmatrix} \mathcal{I}_{xx} & \mathcal{I}_{xy} & \mathcal{I}_{xz} \\ \mathcal{I}_{yx} & \mathcal{I}_{yy} & \mathcal{I}_{yz} \\ \mathcal{I}_{zx} & \mathcal{I}_{zy} & \mathcal{I}_{zz} \end{bmatrix}$$

where  $\mathcal{I}_{\alpha\beta}(\mathbf{x})$  denote regularized derivatives of the image  $I(\mathbf{x})$ , which are obtained by convolving the image with the derivatives of the Gaussian kernel at scale  $\sigma$  [36], [37].

$$\begin{aligned} \mathcal{I}_{\alpha\beta}(\mathbf{x}) &\triangleq \sigma^2 \frac{\partial^2 G(\mathbf{x}, \sigma)}{\partial \alpha \partial \beta} * I(\mathbf{x}) \\ G(\mathbf{x}, \sigma) &\triangleq \frac{1}{\sqrt{(2\pi\sigma^2)^3}} e^{-\|\mathbf{x}\|^2/2\sigma^2}. \end{aligned}$$

In the remainder of the paper  $\lambda_k$  will denote the eigenvalue with the  $k$ th smallest magnitude ( $|\lambda_1| \leq |\lambda_2| \leq |\lambda_3|$ ). Under this assumption, Table I summarizes the relations that must hold between the eigenvalues of the Hessian for the detection of different structures. In particular, a pixel belonging to a vessel region will be signaled by  $\lambda_1$  being small (ideally zero) and  $\lambda_2$  and  $\lambda_3$  being large and of equal sign (the sign is an indicator of brightness/darkness). The respective eigenvectors correspond to singular directions:  $\hat{\mathbf{u}}_1$  indicates the direction along the vessel (minimum intensity variation) and  $\hat{\mathbf{u}}_2$  and  $\hat{\mathbf{u}}_3$  form a basis for the orthogonal plane.

Based on these observations, we developed a discriminant function [18] that enhances tubular structures while reducing the effect of other morphologies. The discriminant function

TABLE I  
POSSIBLE PATTERNS IN 3-D BASED ON HESSIAN EIGENANALYSIS

$\lambda_1$	$\lambda_2$	$\lambda_3$	orientation pattern
N	N	N	noisy, no preferred direction
L	L	H-	plate-like structure (bright)
L	L	H+	plate-like structure (dark)
L	H-	H	tubular structure (bright)
L	H+	H+	tubular structure (dark)
H-	H	H-	blob-like structure (bright)
H+	H+	H+	blob-like structure (dark)

can be expressed as

$$\mathcal{V}(\mathbf{x}, \sigma) \triangleq \begin{cases} 0 & \text{if } \lambda_2 > 0 \text{ or } \lambda_3 > 0, \\ \left[ 1 - \exp\left(-\frac{\mathcal{R}_A^2}{2\alpha^2}\right) \right] \exp\left(-\frac{\mathcal{R}_B^2}{2\beta^2}\right) & \cdot \left[ 1 - \exp\left(-\frac{\mathcal{S}^2}{2c^2}\right) \right] \text{ otherwise} \end{cases} \quad (2)$$

$$\mathcal{R}_A \triangleq \frac{|\lambda_2|}{|\lambda_3|}, \quad \mathcal{R}_B \triangleq \frac{|\lambda_1|}{\sqrt{|\lambda_2\lambda_3|}}$$

$$\mathcal{S} \triangleq \|\mathcal{H}_\sigma\|_F = \sqrt{\sum_j \lambda_j^2}$$

where  $\mathcal{R}_A$ ,  $\mathcal{R}_B$ , and  $\mathcal{S}$  correspond to local measures of cross-sectional asymmetry, blobness, and degree of image structure [18]. The parameters  $\alpha$ ,  $\beta$ , and  $c$  tune the sensitivity of the filter to deviations in  $\mathcal{R}_A$ ,  $\mathcal{R}_B$ , and  $\mathcal{S}$ , relative to the ideal behavior for a line structure.

In Fig. 1, a typical filter output for a straight vessel model with Gaussian luminance cross-section is shown. The maximum is achieved at the center, while the signal decays smoothly toward the boundaries. This behavior is desirable since it implies that a long-range potential will attract the spline toward the center. Similar results can be derived for other symmetric luminance models which is consistent with results reported on previously proposed filters [22], [24], [25].

Equation (2) explicitly states that the filter response is a function of the scale at which the Gaussian derivatives are computed. The filter is applied at multiple scales that span the range of expected vessel widths according to the imaged anatomy. In order to provide a unique filter output for each pixel, the multiple scale outputs undergo a *scale selection* procedure [27]. This amounts to computing the maximum filter response across scales

$$V(\mathbf{x}) = \max_{\sigma_{\min} \leq \sigma \leq \sigma_{\max}} \mathcal{V}(\mathbf{x}, \sigma)$$

In this way, different vessel sizes will be detected at their corresponding scales and both small and large vessels will be captured with the same scheme. In order to deform the vessel central axis, we chose for the following external energy formulation:

$$\mathcal{E}_{\text{external}}^W = -\frac{1}{\ell} \int_0^1 V(\mathbf{C}(v)) \|\mathbf{C}_v(v)\| dv. \quad (3)$$

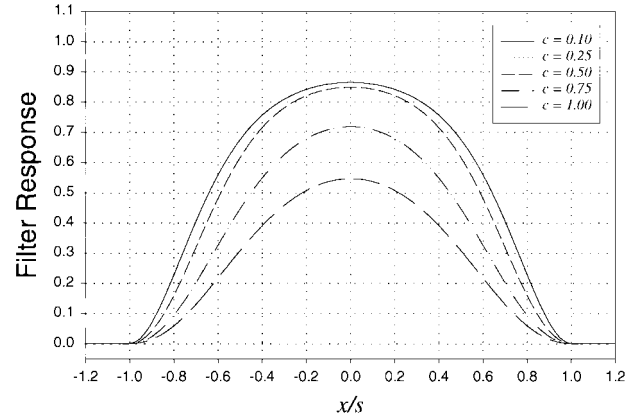


Fig. 1. Typical filter response at single scale. The parameter  $c$  controls the influence of the image contrast and represents the sensitivity of the filter as a percentage of the maximum grey-level value at the center of the vessel. Parameters  $\alpha$  and  $\beta$  control the sensitivity to the vessel radial asymmetry and similarity with a blob-like structure, respectively. In all experiments we use  $\alpha = \beta = 0.5$  and  $c = 0.25 \cdot I_{\max}$ , where  $I_{\max}$  is the maximum luminance value in a region of interest inside the vessel [18]. This filter creates a long-range potential which assures that the maximum is found, even if the initialization of the vessel axis is significantly off.

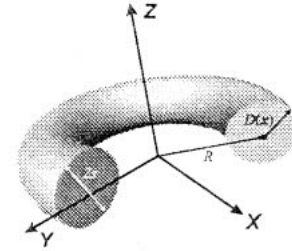


Fig. 2. Toroidal vessel model with outer radius  $R$  and a Gaussian luminance profile of width  $2s$ .  $D(\mathbf{x})$  is the distance between the central axis of the torus and a point  $\mathbf{x}$  in the orthogonal plane.

Minimization of this energy will move the model toward the central axis of the vessel. Note that all terms in (1) are normalized with respect to the length of the vessel axis. This avoids a decrease in the bending and stretching energies, which would result in an artifactual shrinkage.

To investigate the effects of vessel curvature on the response of the filter, we analyzed a toroidal vessel model (Fig. 2) with width  $2s$ , radius  $R$ , and a Gaussian cross-sectional luminance profile

$$I(\mathbf{x}) \triangleq \mathcal{G}(\mathbf{x}, s) = \frac{1}{\sqrt{(2\pi s^2)^3}} e^{-D^2(\mathbf{x})/2s^2} \quad (4)$$

where  $D(\mathbf{x})$  is the distance between the point  $\mathbf{x}$  and the axis of the torus. The Hessian matrix for this model and its eigen decomposition were computed analytically by Krissian *et al.* [20]. We summarize the relevant results in the Appendix. By using the analytic expressions for the different eigenvalues,  $\lambda_k$ , it is possible to analytically evaluate the response of the filter for this vessel model.

Fig. 3 shows the response of the filter in the radial direction. This radius was computed in the  $XZ$  plane. From this figure we conclude that curved vessels only will be distorted when the radius of curvature is of the order of their width (which only occurs in extremely tortuous vessel paths). For vessels

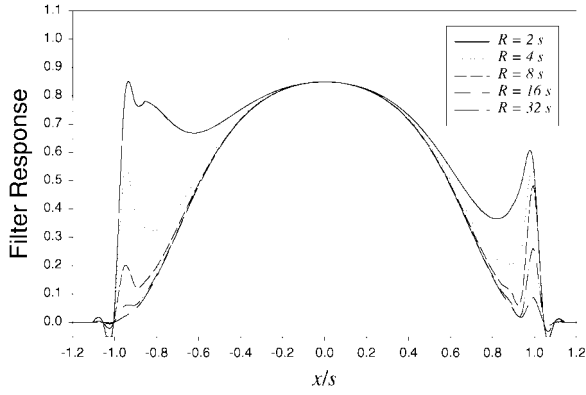


Fig. 3. Simulation of the influence of vessel curvature on filter response at a single scale. For very small radii of curvature, the response of the filter increases toward the boundaries of the vessel, the strongest effect being observed in the direction of the center of curvature. Simulation performed when  $\sigma \rightarrow 0$ . In general, replace  $s \mapsto \sqrt{s^2 + \sigma^2}$ .

with a radius of curvature larger than twice the vessel radius, the filter response is still maximum at the central vessel axis.

We have to note that the proposed filter is not well suited for vessel segmentation on its own, since width estimation is only possible if a model of the cross-sectional luminance profile is known, which varies depending on the acquisition technique and owing to the large variation in patient anatomies.

However, the filter is useful for localization of the central vessel axis since it represents an image feature which smoothly decays from the central vessel axis toward the vessel wall. This image feature provides a long-range potential map which also avoids intervessel response interference, given its zero response beyond vessel boundaries. The response of the filter is only marginally dependent on the curvature of the vessel, which makes it even suited for finding tortuous segments. Finally, as shown in [18], the filter provides excellent noise suppression, which will improve the convergence properties of the central vessel axis model. Noise reduction is both a consequence of the multiscale nature of the filter and the discriminant function (especially the factor containing  $S$ ).

Bifurcations are not incorporated in our local vessel model (a tubular structure). For instance, in bifurcations lying on a plane ( $\Upsilon$ ) there is signal loss in the filtered image around the joint. Such bifurcation behaves halfway between a plate and a tubular structure. The eigenvector with the highest magnitude eigenvalue is directed across the plane defined by the bifurcation. The other two eigenvectors point in the same direction as the branches of the bifurcation, but form an angle of  $90^\circ$  regardless of the bifurcation angle. The magnitude of these two eigenvalues depends on the symmetry of the bifurcation, the bifurcation angle, etc. In the case of a symmetric bifurcation, the magnitude of these eigenvalues will not be zero (as in a plate) but similar to each other and smaller than the third eigenvalue. In this situation, the factors in (2) will only differ from the tubular case in that the term in  $\mathcal{R}_B$  will be smaller. Despite this fact, in the experiments reported in this paper we have not seen that this effect imposes a severe obstacle for a reasonable detection of the vessel axis at the joint.

### B. Diameter Criterion for MRA

Once the central vessel axis is estimated we proceed to capture the boundary of the vessel and, therefore, its width. To this end *a priori* knowledge of the MRA image acquisition is exploited. In a previous work by Hoogeveen *et al.* [38], the factors that can hamper accurate vessel width assessment from MRA were identified. Intrinsic limitations in the image formation/reconstruction process, finite spatial resolution, gridding artifacts, and interpolation determine the achievable accuracy. If the acquisition process is accurately modeled, it is possible to find precise diameter criteria for the three MRA types most frequently used for stenosis grading and/or flow quantification, namely, time-of-flight (TOF), phase-contrast (PC) and contrast-enhanced (CE) MRA. The boundary criteria are defined as a percentage roll-off factor with respect to the maximum luminal MR signal.<sup>2</sup> For TOF and CE MRA the full-width-half-maximum (FWHM) criteria is applied, while for PC MRA the criteria used is the full-width-10%-maximum (FWTM).

These criteria can provide accurate diameter estimates for TOF, PC, and CE MRA if the acquisition meets a number of requirements [38]: 1) resolution is sufficiently high (at least 3 pixels/diameter); 2) saturation due to slow inflow at the borders is limited (only for TOF MRA); and 3) flow artifacts are negligible.

For smaller vessels, diameter quantification is still possible but a more complex model of the acquisition is required which also incorporates tissue properties and parameters of the MR imaging sequence [39].

### C. Vessel Wall Model

The vessel wall is modeled using a tensor product B-spline surface [40]

$$\mathbf{W}(v, u) = \sum_{j=0}^q \sum_{k=0}^r N_{jl}(u) N_{km}(v) \mathbf{P}_{jk}$$

where  $\mathbf{P}_{jk}$  are  $((q+1) \times (r+1))$  control points,  $N_{jl}(u)$  is the  $j$ th B-spline periodic basis function of order  $l$ , and  $u \in [0, 2\pi)$ ,  $N_{km}(v)$  is the  $k$ th B-spline nonperiodic basis function of order  $m$  and  $v \in [0, 1]$ . The parameters  $u$  and  $v$  traverse the surface in the circumferential and longitudinal directions, respectively.<sup>3</sup> We have deliberately coupled the longitudinal parameter ( $v$ ) of the vessel wall and central vessel axis since both span the vessel in the longitudinal direction. This coupling makes it possible to relate central vessel axis points with the corresponding boundary points.

The model can be initialized using a standard CAD technique known as *swept surfaces* [40]. A prototype cross section (*viz.* a circle with a radius equal to the expected average vessel

<sup>2</sup>Compared to [38], the criterion has been made more robust to noise by using as a reference the average of the MR signal in a small neighborhood along the central vessel axis. Although the derivation of the FWHM in [38] was done only for TOF MRA, the same criterion is valid for CE MRA since it is based on assuming a step-like intensity function. This function corresponds to full inflow, an assumption also valid in CE MRA.

<sup>3</sup>For the sake of simplicity, the arguments of the vessel wall model will be henceforth omitted, i.e.,  $\mathbf{W} \triangleq \mathbf{W}(v, u)$ .

width) is swept along the central vessel axis and orthogonal to the curve at every point. In this way, the model is initialized as a flexible cylinder.

To fit the vessel wall model in a smooth fashion we use an approach similar to the one applied in Section II-A, extending the concept from curves to surfaces. The wall model is deformed in a way that maximizes the following integral criterion:

$$\mathcal{E}^W = \mathcal{E}_{\text{external}}^W + \vec{\gamma}_s^W \cdot \vec{\mathcal{E}}_{\text{stretching}}^W + \vec{\gamma}_b^W \cdot \vec{\mathcal{E}}_{\text{bending}}^W \quad (5)$$

where

$$\begin{aligned} \vec{\mathcal{E}}_{\text{stretching}}^W &= \frac{1}{S} \int_0^1 \int_0^{2\pi} \left( \frac{\|\mathbf{W}_v\|^2}{\|\mathbf{W}_u\|^2} \right) \|\mathbf{W}_v \times \mathbf{W}_u\| \, dv \, du \\ \vec{\mathcal{E}}_{\text{bending}}^W &= \frac{1}{S} \int_0^1 \int_0^{2\pi} \left( \frac{2\|\mathbf{W}_{vv}\|^2}{\|\mathbf{W}_{uu}\|^2} \right) \|\mathbf{W}_v \times \mathbf{W}_u\| \, dv \, du \\ S &= \int_0^1 \int_0^{2\pi} \|\mathbf{W}_v \times \mathbf{W}_u\| \, dv \, du \end{aligned}$$

$$\vec{\gamma}_s^W = (\gamma_{sv}^W, \gamma_{su}^W) \quad \vec{\gamma}_b^W = (\gamma_{bvv}^W, \gamma_{bvu}^W, \gamma_{bau}^W)$$

where  $\vec{\gamma}_s^W$  and  $\vec{\gamma}_b^W$  are vectors of weight factors for the internal energy terms. The stretching energy term can be physically interpreted as an approximation to the energy of a thin plate under tension, while the bending energy is related to the rigidity of the deformable surface [35].

So far, the vessel wall model is purely geometric. To further incorporate prior knowledge of the acquisition, let us assume that the maximum of the MR signal is attained at the central vessel axis. Although this assumption might be violated in certain cases, it provides a simplified formulation of the problem that leads to accurate results in most situations. Under this assumption we can cast the diameter criteria of Section II-B into the external energy term of the deformable wall as follows:

$$\mathcal{E}_{\text{external}}^W = \frac{1}{S} \int_0^1 \int_0^{2\pi} \left| \tau_{acq} - \frac{I(\mathbf{W}(v, u))}{I(\mathbf{C}(v))} \right| \cdot \|\mathbf{W}_u \times \mathbf{W}_v\| \, dv \, du \quad (6)$$

where  $\tau_{acq}$  is a threshold that introduces the knowledge about the type of MRA imaging technique. This constant equals 0.5 for TOF and CE MRA and 0.1 for PC MRA (cf. Section II-B).

### III. IMPLEMENTATION ISSUES

#### A. Image Resampling

In order to reduce the effect of gridding artifacts due to the MR image reconstruction, the original image was interpolated to a two-fold larger reconstruction matrix. Based on the properties of the MR image formation process, Du *et al.* [41] showed that partial volume effect in MR can be reduced with *sinc* interpolation. They also suggested an

efficient implementation based on zero-filled interpolation. We have used an approximation to *sinc* interpolation based on cubic convolution, which is computationally more efficient than zero-filled interpolation and has extremely good *sinc* approximating properties [42].

#### B. Scenario for 3-D Interaction

Although deformable models have been shown to be useful in a variety of 3-D applications, it has been recognized that initialization and interaction in 3-D is, in general, an open problem. On the other hand, it has also been acknowledged that proper initialization is a requirement for good convergence of most deformable model approaches.

We suggest the use of an isosurface rendering for interactively inspecting the vascular anatomy and for selecting the target segment in which the quantitative analysis will be performed. In Fig. 4, the steps of the procedure are highlighted. First, an isosurface rendering of the original angiogram is generated [Fig. 4(a)]. This is accomplished using *marching cubes* [43]. We are aware that this step implies the selection of a threshold. However, we recall that the only purpose of this step is to provide a support for visual interaction. Second, the operator defines a vessel segment by clicking two points on the isosurface which define the end-points of a *geodesic* path.<sup>4</sup> This path is used for initializing the central vessel axis after it has been converted into B-spline form using a least squares approximation [Fig. 4(b)]. Third, once the central vessel axis has been determined, the vessel wall must be initialized. This can be accomplished with no extra user interaction by computing a radius function as the distance between the central vessel axis and the geodesic path. Since the geodesic path lies somewhere close to the vessel boundary, its distance to the vessel axis provides a rough approximation of the vessel radius at every point along the center line. This function is subsequently used to modulate the radius while sweeping a circular cross section along the vessel axis [Fig. 4(c)]. Fig. 4(d) shows the final result of the fitting procedure. Once the model is obtained, a report can be generated indicating cross-sectional area as well as minimum, maximum, and average vessel diameter along the vessel axis.

#### C. Model Optimization

Having specified the energy functionals for the central vessel axis and vessel wall, we must choose how to optimize the degrees of freedom of these geometric models (the control points of the B-spline curve/surface).

The optimization is performed in two steps. First, the central vessel axis is deformed according to (1). Once it converges, the initial guess of the vessel wall is generated by sweeping along the central vessel axis. Subsequently, the model of the vessel wall is deformed to reach the vessel boundary following (5). The deformation process of both the central vessel axis and vessel wall is performed using the conjugate gradient [44] algorithm with analytical derivatives. The energy integrals

<sup>4</sup> Given two points on a surface, a *geodesic* is defined as the shortest path on the surface connecting them.

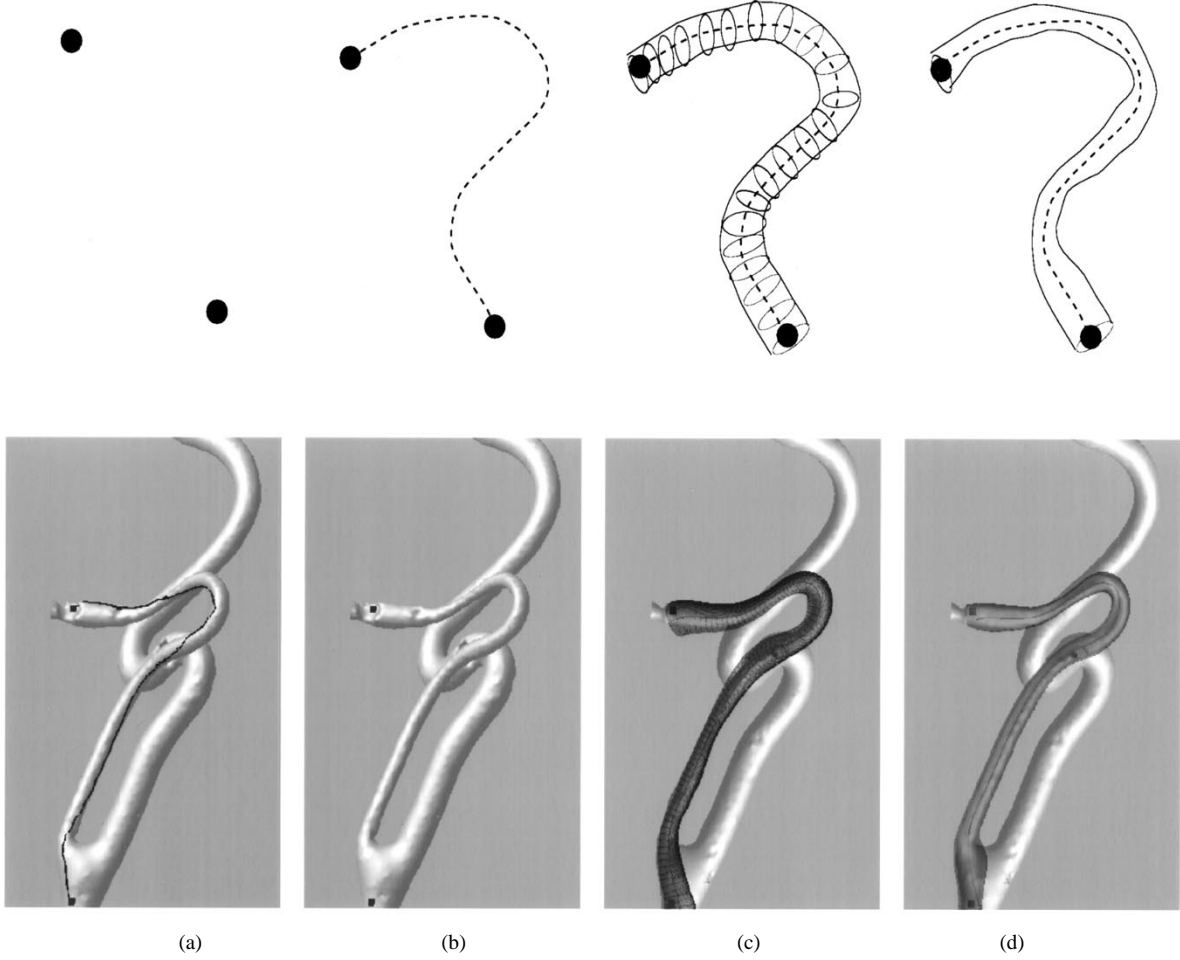


Fig. 4. Interaction scenario. (a) A user initializes two (or more) points on the iso-surface generated from the original image. (b) From these seeds, a geodesic path is computed. (c) The geodesic path is deformed until the central vessel axis is determined. Using the distance between the newly obtained vessel axis and the original geodesic, a circular cross section is swept along the axis to generate an initialization of the vessel wall model. (d) Vessel wall (after deformation) and central vessel axis. Note that each model deforms using a different external energy [cf. (3) and (6)].

involved in (1) and (5) were computed numerically using Gauss–Legendre quadrature formulas [44].

To avoid surface self intersections during the deformation process of the wall model, we constrain the movement of the control points. Each subset of control points sharing the same column index (i.e., affecting the same circumferential wall strip) are constrained to move in a plane perpendicular to the central vessel axis (Fig. 5). Mathematically

$$\mathbf{P}_{jk_o} = \mathbf{C}(v_{k_o}) + r_{jk_o} \cos \theta_{jk_o} \mathbf{N}(v_{k_o}) + r_{jk_o} \sin \theta_{jk_o} \mathbf{B}(v_{k_o})$$

where  $\mathbf{C}$ ,  $\mathbf{N}$ , and  $\mathbf{B}$  are the central vessel axis coordinates and the central vessel axis normal and binormal vectors of its Frenet frame at parameter value  $v_{k_o}$ .<sup>5</sup> In this expression,  $(r_{jk}, \theta_{jk})$  represents the location of the control point  $\mathbf{P}_{jk}$  in polar coordinates of the local cross-sectional plane. By restricting  $r_{jk} \geq 0$  and  $\theta_{j-1,k} \leq \theta_{j,k} \leq \theta_{j+1,k}$ ,<sup>6</sup> The central vessel axis is enforced to lie inside the boundaries of the vessel wall.

<sup>5</sup> Here,  $v_{k_o}$  is the parametric value,  $v$ , where the basis function  $N_{k_o m}(v)$  is maximal. This corresponds to the parameter value for which  $\mathbf{P}_{jk_o}$  have maximum influence on the curve for all  $j$ .

<sup>6</sup> In this expression  $j$  denotes a cyclic index with period  $q$ .

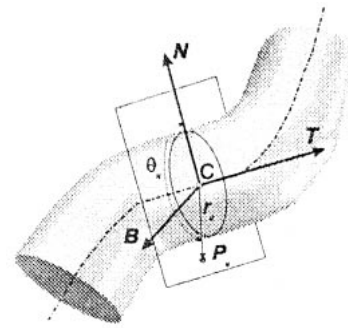


Fig. 5. The control points of the vessel wall model are restricted to move in a plane orthogonal to the vessel axis.

#### D. Geometric Modeling

In Table II, the parameters of the vessel model for the carotid bifurcation segment are summarized. Note that the internal energy weights are small (the external energy range typically from zero to one) such that, unless the model is subjected to large stretching or bending deformations, it mainly will be guided by the external energy term. Problems often attributed to deformable models are the *ad hoc* nature of the

TABLE II  
GEOMETRIC MODEL PARAMETERS

Vessel Axis		
$n$	B-spline curve order	3
$s + 1$	Number of control points	15
$\gamma_s^C$	Stretching weight	$0.1/E_s^C$
$\gamma_b^C$	Bending weight	$0.05/E_b^C$
Vessel Wall		
$l$	B-spline surface order (circ.)	3
$q + 1$	Number of control points (circ.)	5
$m$	B-spline surface order (long.)	2
$r + 1$	Number of control points (long.)	25
$\gamma_{su}^W$	Stretching weight (circ.)	$0.1/E_{su}^W$
$\gamma_{sv}^W$	Stretching weight (long.)	$0.1/E_{sv}^W$
$\gamma_{buu}^W$	Bending weight (circ.)	$0.05/E_{buu}^W$
$\gamma_{bvu}^W$	Bending weight (mixed)	$0.05/E_{bvu}^W$
$\gamma_{bvv}^W$	Bending weight (long.)	$0.05/E_{bvv}^W$

selection of weights and the fact that they have to be tuned for each application (which most of the time means each image). In our implementation we chose to normalize each internal energy term with respect to its value in the initialization. By proceeding in this way, we obtain internal energy terms that are dimensionless and that were suited for all the experiments we carried out (Table II). Moreover, internal energy terms and the external energy are now commensurable and it is possible to incorporate an extra coefficient in the weights that represents their relative contribution to the total energy. Note that using such normalization factors is justified if the initial shape of the models is representative of their final shape, which is ensured by our initialization procedure.

#### IV. IN VITRO EVALUATION

##### A. Phantom and Image Acquisition

In order to assess the performance of the algorithm we addressed the problem of diameter measurements for stenosis grading in an MR compatible carotid bifurcation phantom with an asymmetric stenosis (R. G. Shelley Ltd., North York, Ontario). A photograph of this phantom is shown in Fig. 6. The phantom is embedded in a rigid transparent acrylic and manufactured to reproduce normal dimensions in the human vasculature [45].

Images were acquired on a 1.5-T MR imaging system (Philips Gyroscan ACS-NT, PowerTrak 6000 gradients, Philips Medical Systems, Best, The Netherlands) with a quadrature head-neck receiver coil. Imaging parameters for experiments on the carotid bifurcation phantom were as follows. Three-dimensional TOF MRA acquisition: echo time (TE) 1.9 ms, repetition time (TR) 25.0 ms and flip angle ( $\alpha$ ) 15°, slice thickness 1.0 mm. CE MRA acquisition: TE 2.0 ms, TR 6.6 ms,  $\alpha$  40°, slice thickness 1.0 mm. Both acquisitions: FOV 256 mm, scan matrix 256 × 256. First-order flow compensation was applied in the TOF MRA acquisition. The flow was regulated by a computer-controlled pump (Quest Image Inc., London, Ontario). Water was guided through the phantom with constant velocity (5 ml/s) and a

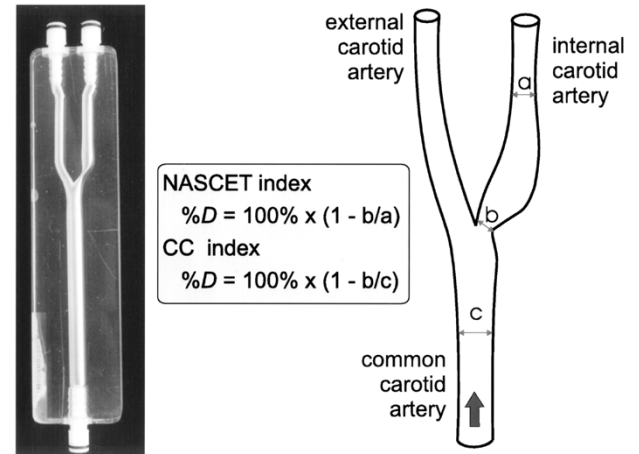


Fig. 6. Carotid bifurcation phantom with a 70% asymmetric stenosis (Courtesy of R. G. Shelley Ltd., North York, Ontario, Canada). Two indexes (NASCET and CC) are usually used to quantify stenosis in the carotids with different reference diameters.

long inlet length was taken to assure that laminar flow was established. For CE MRA acquisitions, a 5 mM solution of gadopentetate dimeglumine (Magnevist, Schering, Berlin, Germany) was used under the same flow conditions as the TOF MRA acquisition.

##### B. Performance Assessment

We assessed the performance of the algorithm in comparison with two human operators and the ground truth as the gold standard. To this end, the stenosis in the carotid phantom was graded by two experts following a manual procedure. This is based on visual inspection of vessel dimensions on a multiplanar reformatted (MPR) image. The reformatting was generated by manually drawing a central vessel axis and subsequently computing the plane perpendicular to it. This procedure was performed on a clinical workstation (EasyVision, Philips Medical Systems, Best, The Netherlands).

In order to compare the measurements provided by the experts and the results obtained with our algorithm, a measurement protocol was established. The degree of stenosis was computed using the NASCET index [1]. A second measure of stenosis, taken relative to the common carotid artery (CC index) was also computed for comparison.<sup>7</sup> To incorporate the variability inherent to the definition of the stenosis diameter, our protocol required that the experts measured the distal diameter at  $D = 15$  mm from the center of the stenosis and repeated the measurements for two other successive planes separated by  $d = 5$  mm. For each plane, the minimum and maximum observed diameters were recorded. All measurements were done twice by the same expert, with enough delay to disregard any possible bias in the second measurement. The average stenosis grade and the 99% confidence interval (CI) were computed for each observer, for both observers, and for the proposed algorithm. The statistics of stenosis grading with the model-based approach were computed, based on all possible values of the degree of stenosis for a region of 2 mm

<sup>7</sup>The definition of the two indexes can be found in the inset of Fig. 6.

TABLE III  
STENOSIS GRADING SUMMARY: CAROTID BIFURCATION PHANTOM WITH ASYMMETRIC STENOSIS.  
WITHIN ( $WO_1$ ,  $WO_2$ ) AND BETWEEN OBSERVER ( $BO_{12}$ ) STATISTICS OF TWO EXPERTS COMPARED TO THE MODEL-BASED APPROACH ( $MB$ )

Criterion	Code	$WO_1$	$WO_2$	$BO_{12}$	$MB$
		% $D \pm CI_{99\%}$	% $D \pm CI_{99\%}$	% $D \pm CI_{99\%}$	% $D \pm CI_{99\%}$
CC (78.5% $\pm$ 0.65%)	3D-TOF-1.0	69.8 $\pm$ 3.47	62.8 $\pm$ 5.30	66.3 $\pm$ 3.20	76.7 $\pm$ 0.20
	3D-CEA-1.0	68.4 $\pm$ 1.40	62.8 $\pm$ 4.10	65.6 $\pm$ 2.30	76.0 $\pm$ 0.22
NASCET (69.2% $\pm$ 0.95%)	3D-TOF-1.0	55.2 $\pm$ 4.10	39.1 $\pm$ 7.52	47.2 $\pm$ 5.21	67.6 $\pm$ 0.14
	3D-CEA-1.0	55.8 $\pm$ 3.30	48.3 $\pm$ 5.25	52.1 $\pm$ 3.38	65.9 $\pm$ 0.19

Stenosis indexes according to CC and NASCET criterion. The true values are indicated in the first column.

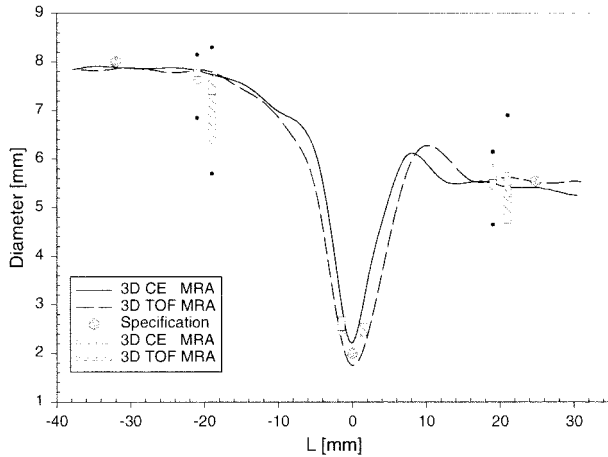


Fig. 7. Average diameter of the carotid bifurcation phantom. The average is performed over all pairs of antipodal points at a given point along the vessel axis. The diameter of the phantom (estimated from phantom specifications [45]) and the box-and-whisker plots corresponding to the measurements performed by two experts are also included (average between min and max diameter). For the sake of clarity, the average abscissa of each pair of boxes corresponds to the place where the measurements were carried out.

around the stenosis and a region of  $2d = 10$  mm centered at a distance  $D + d = 20$  mm from the stenosis. This yields a measure of stability of the model-based measurements in the region where the operators performed the manual analysis.

## V. RESULTS

### A. Carotid Bifurcation Phantom

In Fig. 7, the average diameter measurements are shown (the average diameter in the orthogonal plane at a given location along the central vessel axis). For comparison purposes it also includes, at three points, diameter values from the specifications of the phantom [45]. From this figure it is apparent that manual assessment suffers from a large variability. This can be attributed to factors such as the window leveling settings of the MR console and the subjective criterion that each radiologist uses to define the boundaries of the vessel. This is further aggravated by the fact that even circular vessels will show different apparent cross sections [38], depending on the effective resolution (the number of pixels per diameter).

In Table III, the statistics of the stenosis grading are summarized. The phantom we used has a stenosis index of 69.2% according to NASCET and 78.5% according to CC [45]. The table shows that the method improves stenosis grading, with an

absolute error smaller than 3.3% for both criteria. Moreover, reproducibility is much better in the model-based approach.

### B. Illustration of the Algorithm on Patient Data

In Fig. 8, results of the algorithm on patient data are shown. Fig. 8(a) and 8(b) shows MIP's of 3-D TOF angiograms of the left (mild stenosis) and right (severe stenosis) carotids of the same patient, respectively. Fig. 8(c) shows the left carotids of a second patient with a mild stenosis. The datasets are part of an ongoing trial in our hospital to compare several imaging techniques for stenosis grading. The parameters of the 3-D TOF MRA sequence were as follows: TR 30.6 ms, TE 6.8 ms,  $\alpha$  15°, with a pixel size of 0.5 mm, slice thickness of 1.0 mm, and a slice gap of 0.5 mm.

A summary of quantitative results for stenosis grading of these data is given in Table IV. In the same table, stenosis grades assessed by a radiologist from MIP's of 3-D TOF MRA images and 2-D DSA projections are also included for comparison. To illustrate that in our model there is no assumption of circularity, we show in Fig. 9 several shape characteristics, such as the minimum, maximum and average diameter, and cross-sectional area measurements for the example of Fig. 8(a). Our model based method correlates better with DSA, which is the gold standard in many radiological studies [7]–[9], than the manual assessment from 3-D TOF.

Flow artifacts were small in the *in vitro* experiments. In patient data, however, the algorithm performs well for nonsevere stenosis and/or when flow artifacts are negligible. This was one of the assumptions for the validity of the FWHM criterion. In Fig. 8(b) an example of a severe stenosis is shown. Post-stenotic flow artifacts hampered good fit of the model at the stenosis and distal to it. At the stenosis, the luminal intensity has a cloudy appearance and the vessel axis in this region is mainly guided by the internal energy term which forces the axis model to extrapolate the nonstenosed vessel axis. Even when the degree of stenosis occasionally agrees with the expert's grading based on DSA, if the vessel axis falls outside the vessel lumen, the vessel wall determination cannot be accurate. We therefore considered this as a failure case (noted between parenthesis). When images contain large flow artifacts, manual assessment of the degree of stenosis is also difficult and more susceptible to intraobserver variability.

## VI. DISCUSSION

We devised a method to perform quantitative diameter assessment with subvoxel precision. The method shares some



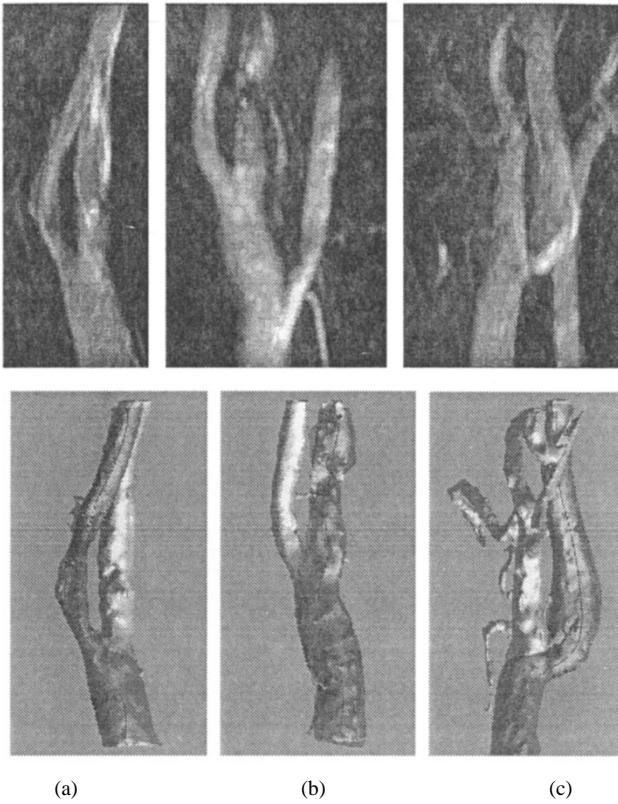


Fig. 8. Stenosed left internal carotid arteries (ICA). The top row shows MIP's of 3-D TOF datasets of the ICA. (a) and (b) correspond to the left and right ICA of the same patient and (c) corresponds to the left ICA of a second patient. In the lower row we show the corresponding vessel models. The models are quite accurate for the two left ICA cases shown. For the right ICA, however, the presence of flow artifacts close to the severe stenosis (90% graded on MRA and 53% on DSA according to NASCET) precluded following the vessel axis.

TABLE IV  
IN-VIVO STENOSIS GRADING OF THE CAROTIDS  
MANUAL (3-D TOF AND DSA) AND MODEL-BASED (3-D TOF)

Patient	3D TOF %D	DSA %D	3D TOF (MB) %D
A - L ICA (Fig. 8(a))	28%	36%	38%
A - R ICA (Fig. 8(b))	90%	53%	NA Is
B - L ICA (Fig. 8(c))	53%	34%	28%
B - R ICA	74%	53%	49%

The stenosis index follows the NASCET criterion.  
L = left R = right

features with multiscale vessel enhancement algorithms based on eigenvalue analysis of the Hessian matrix originally proposed by Koller and co-workers [19] and further modified by Sato *et al.* [24], [25] and Lorenz *et al.* [22]. However, in these approaches a segmentation of the vasculature was obtained by estimating the vessel width as a function of the scale of maximum response. The accuracy of these algorithms is therefore *a priori* limited by the discretization of the scale parameter. This limits the applicability of these methods to give a general overview of the vasculature. For stenosis grading a more accurate approach is required.

Our method performs quantitative analysis based on the original 3-D images. It is known from the literature [7]–[9] that

assessment of stenosis based on MIP's tends to overestimate the degree of stenosis. Table IV nicely exemplifies this fact. This artifact is not only attributed to flow related signal loss, but also to the image processing involved in generating the MIP's [4]–[6]. In order to eliminate this artifact, some authors have argued in favor of methods that avoid the MIP operation. Anderson *et al.* [9], for instance, have suggested grading stenoses based on the source images. De Marco *et al.* [7] resourced to MPR images which allow for better visualization of the vessel lumen in a plane orthogonal to the vessel axis. De Marco *et al.* [7] compared stenosis grading based on MIP's and MPR images of 3-D TOF MR angiograms, and used intraarterial angiography (DSA) as a standard of reference. They reported a statistically significant difference between MIP's and DSA scores with an average absolute error  $\sim 9\%$  ( $SD \sim 14\%$ ). MPR images provided a better agreement with DSA and a negligible bias. Although this study suggests the potential benefit of MPR-based diagnosis, generation and inspection of MPR's is relatively time consuming. Our method shares the basic idea behind MPR-based measurements. We apply an objective vessel diameter criterion in planes orthogonal to the vessel axis, which is therefore similar to the radiologist's when analyzing MPR images. On the other hand, the method is objective (does not depend on window leveling settings) and requires little interaction. We hypothesize that this correspondence between our method and MPR-based diagnosis is responsible for the smaller bias in our method (versus DSA) compared to manual assessment based on MIP's (versus DSA). This hypothesis, however, must be further evaluated on a larger number of patients. The differences observed between our model-based method and DSA are close to the figures reported in the literature for intraobserver differences using DSA. Anderson *et al.* [9], e.g., reported intraobserver absolute differences of 5%, but they can be as high as 30% [46]. Therefore, the difference between the model-based method and DSA may not be statistically significant. Compared to measurements based on DSA, our method avoids the difficulties of selecting a suitable projection angle [47] by providing true 3-D measurements.

We have applied an algorithm which estimates the boundaries of the vessels using knowledge of the MRA image acquisition technique. This is a distinguishing property of our method compared to other previously published multiscale techniques [17]–[25]. Whereas the algorithm contains a scale selection procedure in the determination of the central vessel axis, this does not influence the diameter assessment. Moreover, our model based on splines can model noncircular vessel cross sections. Although often it is assumed that vessels have a circular cross section, *ex vivo* measurements [28] have shown that this assumption is rather simplistic and, especially at the stenosis, a wide variety of geometric shapes can be observed. Elgersma and coworkers [29] have supported this idea based on *in vivo* measurements from multiple projections of 3-D rotational angiography (RA) images and concluded that this imposes a severe limitation to measurements performed on (only two or three) 2-D projections. Three dimensional approaches, such as the one presented in this work, provide a basis for both the description of the actual cross-sectional

shape and its quantification. They also allow definition of stenosis indexes based on cross sectional area reduction (cf. Fig. 9), which are more robust than those based on diameter reduction.

The method has been illustrated on phantom and patient data. In the phantom data the method obtained diameter and stenosis measurements with an accuracy which was considerably better than the experts. Although the results on the clinical data are promising, a thorough validation is still required.

Other aspects of the methodology need further research. The influence of vessel bifurcations in the deformation of the model must be better understood. Apparently, if the stenosis is reasonably away from the flow divider, stenosis assessment can be performed with good accuracy. This was observed, for instance, in the carotid bifurcation phantom and in the patient data of Fig. 8(a). However, it is clear that with a tubular model there will always be a region where diameter measurements will be an extrapolation of the diameters before and after the bifurcation [see Fig. 8(c)]. Note, however, that in such situations a radiologist would also have to mentally perform such an extrapolation.

The method performed poorly in the presence of large flow artifacts [see Fig. 8(b)]. This is a potential limitation of the methodology when applied to 3-D TOF MRA, since stenoses are usually regions of disturbed flow. In such situations, however, manual assessment of stenosis is also delicate. Our method is, in principle, applicable to other techniques such as CE or blood pool agent (BPA) MRA, which are less sensitive to disturbed flow. We are currently starting up a study that will evaluate our methodology in a larger set of CE MRA images.

Finally, it would be interesting to analyze a large set of vascular segments and study the influence of the number of control points of the B-spline representation on the accuracy of the measurements. This analysis will probably give a basis for building a database of models tailored to different applications (carotids, aorta, etc.). Each model would consist not only of the optimum number of degrees of freedom of the geometric model but also suitable weights for the energy terms. It is known that the weighting factors present in the formulation of deformable models are generally chosen in an *ad hoc* fashion. However, for a given application, suitable values can be found based on the analysis of a representative set of data. This is especially feasible in medical applications, where images are acquired according to strict protocols.

#### APPENDIX: ANALYTICAL MODEL OF A TOROIDAL VESSEL

Krissian *et al.* [20] proposed a vessel model with a Gaussian luminance profile. Although this is a simplification, it allows us to carry out some analytical simulations that would be otherwise quite cumbersome, if at all possible. In this appendix we summarize the results for a toroidal model. An analogous formulation can be derived for a cylindrical model [20].

The vessel is modeled by a torus whose outer circle is parallel to the plane  $XY$  and has radius  $R$ . The small circle has radius  $s$  (Fig. 2). For the toroidal model of (4), the distance from a point  $\mathbf{x} = (x, y, z)$  to the axis of the torus is

$$D(\mathbf{x}) = \sqrt{(R - \sqrt{x^2 + y^2})^2 + z^2}.$$

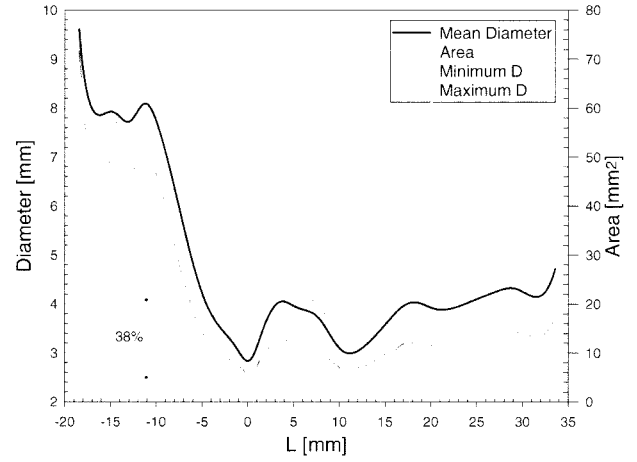


Fig. 9. Stenosed ICA. Area and (min/max/average) diameter measurements of the left ICA along the vessel axis for the patient in Fig. 8(a). Stenosis index computed based on the maximal vessel narrowing and the average distal diameter.

From the circular symmetry around the  $OZ$  axis we can choose  $y = 0$  and  $x > 0$ . The Hessian matrix can be expressed as

$$\mathcal{H} = \frac{I(\mathbf{x})}{s^4} \begin{bmatrix} (R-x)^2 - s^2 & 0 & -z(R-x) \\ 0 & \frac{(R-x)s^2}{x} & 0 \\ -z(R-x) & 0 & z^2 - s^2 \end{bmatrix}. \quad (7)$$

Eigenvalue analysis of (7) results in

$$\begin{aligned} \lambda_1 &= -\frac{I(\mathbf{x})}{s^2} \left( \frac{x-R}{x} \right) & \mathbf{\bar{u}}_1 &= (0, 1, 0) \\ \lambda_2 &= -\frac{I(\mathbf{x})}{s^2} \left[ 1 - \left( \frac{D(\mathbf{x})}{s} \right)^2 \right] & \mathbf{\bar{u}}_2 &= (x-R, 0, z) \\ \lambda_3 &= -\frac{I(\mathbf{x})}{s^2} & \mathbf{\bar{u}}_3 &= (z, 0, R-x) \end{aligned}$$

where  $\lambda_i$  and  $\mathbf{\bar{u}}_i$  denote eigenvalues and eigenvectors, respectively.

#### ACKNOWLEDGMENT

The authors acknowledge the cooperation of Dr. F. Gerritsen and S. Lobregt from EasyVision Advanced Development, Philips Medical Systems BV, Best, The Netherlands. They would like to thank Dr. K. L. Vincken and G. van Hoorn for technical support. P. Lavoie from the School of Information Technology and Engineering, University of Ottawa, Canada, kindly contributed to the implementation of the B-spline models. Dr. O. E. H. Elgersma provided the 3-D TOF MRA datasets of the carotids. Dr. J. Bakker and Dr. J. M. Scheffers performed the manual measurements. The authors would also like to express their gratitude to the reviewers for their suggestions for improving the presentation of this work.

#### REFERENCES

- [1] North American Symptomatic Carotid Endarterectomy Trial (NASCET) Steering Committee, "North American symptomatic carotid endarterectomy trial," *Stroke*, vol. 22, pp. 711-720, 1991.
- [2] European Carotid Surgery Trialists' Collaborative Group, "Randomised trial of endarterectomy for recently symptomatic carotid stenosis: Final

- results of the MRC European Carotid Surgery (ECST)," *Lancet*, vol. 351, pp. 1379–87, 1998.
- [3] European Carotid Surgery Trialists' Collaborative Group, "Endarterectomy for moderate symptomatic carotid stenosis: Interim results from the MRC European Carotid Surgery Trial," *Lancet*, vol. 347, pp. 1591–1593, 1996.
  - [4] H. Cline, C. Dumoulin, W. Lorensen, S. Souza, and W. Adams, "Volume rendering and connectivity algorithms for MR angiography," *Magn. Res. Med.*, vol. 18, pp. 384–394, 1991.
  - [5] C. M. Anderson, J. S. Saloner, D. Tsuruda, L. G. Shapeero, and R. E. Lee, "Artifacts in maximum-intensity-projection display of MR angiograms," *Amer. J. Roentgenol.*, vol. 154, pp. 623–629, 1990.
  - [6] S. Schreiner, C. B. Paschal, and R. L. Galloway, "Comparison of projection algorithms used for the construction of maximum intensity projection images," *J. Comput. Assisted Tomogr.*, vol. 20, no. 1, pp. 56–67, Jan. 1996.
  - [7] J. K. De Marco, G. M. Nesbit, G. E. Wesbey, and D. Richardson, "Prospective evaluation of extracranial carotid stenosis: MR angiography with Maximum-Intensity Projections and Multiplanar Reformation compared with conventional angiography," *Amer. J. Roentgenol.*, vol. 163, pp. 1205–12, Nov. 1994.
  - [8] J. E. Heiserman, B. P. Drayer, P. J. Keller, and E. K. Fram, "Intracranial vascular stenosis and occlusion: Evaluation with three-dimensional Time-of-Flight MR angiography," *Radiology*, vol. 185, pp. 667–73, Dec. 1992.
  - [9] C. M. Anderson, R. E. Lee, D. L. Levin, S. de la Torre Alonso, and D. Saloner, "Measurement of internal carotid artery stenosis from source MR angiograms," *Radiology*, vol. 193, pp. 219–226, Oct. 1994.
  - [10] Y. P. Du and D. L. Parker, "Vessel enhancement filtering in three-dimensional MR angiography," *J. Magn. Res. Imag.*, vol. 5, no. 3, pp. 353–359, 1995.
  - [11] Y. P. Du and D. L. Parker, "Vessel enhancement filtering in three-dimensional MR angiograms using long-range signal correlation," *J. Magn. Res. Imag.*, vol. 7, no. 2, pp. 447–450, 1997.
  - [12] M. M. Orkisz, C. Bresson, I. E. Magnin, O. Champin, and P. C. Douek, "Improved vessel visualization in MR angiography by nonlinear anisotropic filtering," *Magn. Res. Med.*, vol. 37, no. 6, pp. 914–9, June 1997.
  - [13] H. Chen and J. Hale, "An algorithm for MR angiography image enhancement," *Magn. Res. Med.*, vol. 33, no. 4, pp. 534–40, Apr. 1995.
  - [14] D. L. Wilson and J. C. A. Noble, "Segmentation of cerebral vessels and aneurysms from MR angiography data," in *Proc. Information Processing Medical Imaging*, Poultny, VT, June 1997, pp. 423–428.
  - [15] R. Kutka and S. Stier, "Extraction of line properties based on direction fields," *IEEE Trans. Med. Imag.*, vol. 15, pp. 51–58, Jan. 1996.
  - [16] C. Steger, "An unbiased detector of curvilinear structures," *IEEE Trans. Pattern Anal. Machine Intell.*, vol. 20, pp. 113–125, Feb. 1998.
  - [17] S. Aylward, E. Bullitt, S. Pizer, and D. Eberly, "Intensity ridge and widths for tubular object segmentation and description," in *Proc. IEEE/SIAM Workshop Mathematical Methods Biomedical Image Analysis*, 1996, pp. 131–8.
  - [18] A. F. Frangi, W. J. Niessen, K. L. Vincken, and M. A. Viergever, "Multiscale vessel enhancement filtering," in *MICCAI98 Medical Image Computing & Computer-Assisted Intervention* (Lecture Notes in Computer Science), A. Colchester, W. M. Wells, and S. Delp, Eds. New York: Springer-Verlag, 1998, vol. 1496, pp. 130–137.
  - [19] Th. Koller, G. Gerig, G. Székely, and D. Dettwiler, "Multiscale detection of Curvilinear Structures in 2-D and 3-D Image Data," in *Proc. Fifth Int. Conf. Computer Vision*. New York: IEEE Computer Society, 1995, pp. 864–869.
  - [20] K. Krissian, G. Malandain, and N. Ayache, "Model-based multiscale detection and reconstruction of 3D vessels," INRIA, RR 3442.
  - [21] K. Krissian, G. Malandain, R. Vaillant, N. Ayache, and Y. Troussset, "Model based detection of tubular structures in 3D images," INRIA Sophia Antipolis, RR 3736, July 1999.
  - [22] C. Lorenz, I.-C. Carlsen, T. M. Buzug, C. Fassnacht, and J. Weese, "Multi-scale line segmentation with automatic estimation of width, contrast and tangential direction in 2D and 3D medical images," in *CVRMed-MRCAS'97*, (Lecture Notes in Computer Science), J. Troccaz, E. Grimson, and R. Mösges, Eds. Berlin, Germany: Springer-Verlag, 1997, pp. 233–242.
  - [23] R. Poli and G. Valli, "An algorithm for real-time vessel enhancement and detection," *Comput. Methods Programs Biomed.*, vol. 52, no. 1, pp. 1–22, 1996.
  - [24] Y. Sato, S. Nakajima, H. Atsumi, T. Koller, G. Gerig, S. Yoshida, and R. Kikinis, "3D multi-scale line filter for segmentation and visualization of curvilinear structures in medical images," in *CVRMed-MRCAS'97*, (Lecture Notes in Computer Science) J. Troccaz, E. Grimson, and R. Mösges, Eds. Berlin, Germany: Springer-Verlag, 1997, pp. 213–222.
  - [25] Y. Sato, S. Nakajima, N. Shiraga, H. Atsumi, S. Yoshida, T. Koller, G. Gerig, and R. Kikinis, "Three-dimensional multi-scale line filter for segmentation and visualization of curvilinear structures in medical images," *Med Image Anal.*, vol. 2, no. 2, pp. 143–168, June 1998.
  - [26] P. E. Summers, A. H. Bhalerao, and D. J. Hawkes, "Multiresolution, model-based segmentation of MR angiograms," *J. Magn. Reson. Imag.*, vol. 7, pp. 950–957, 1997.
  - [27] T. Lindeberg, "Feature detection with automatic scale selection," *Int. J. Comput. Vision*, vol. 30, no. 2, pp. 79–116, Nov. 1998.
  - [28] X. M. Pan, D. Saloner, L. M. Reilly, J. C. Bowersox, S. P. Murray, C. M. Anderson, G. A. Gooding, and J. H. Rapp, "Assessment of carotid artery stenosis by ultrasonography, conventional angiography, and magnetic resonance angiography: Correlation with *ex vivo* measurements of plaque stenosis," *J. Vasc. Surg.*, vol. 21, pp. 82–89, 1995.
  - [29] O. E. H. Elgersma, P. C. Buijs, A. F. J. Wüst, Y. van der Graaf, B. C. Eikelboom, and W. P. Th. M. Mali, "Assessment of maximum internal carotid artery stenosis: Rotational vs. conventional intra arterial digital subtraction angiography," *Radiology*, in press, 1999.
  - [30] J. H. C. Reiber and P. W. Serruys, "Quantitative coronary angiography," in *Cardiac Imaging-A Companion to Braunwald's Heart Disease*, M. L. Marcus et al., Eds. Philadelphia, PA: Saunders, 1991.
  - [31] A. K. Klein, F. Lee, and A. A. Amini, "Quantitative coronary angiography with deformable spline models," *IEEE Trans. Med. Imag.*, vol. 16, pp. 468–482, Oct. 1997.
  - [32] G. Farin, *Curves and Surfaces for Computer Aided Geometric Design: A Practical Guide*, 2nd ed. New York: Academic, 1990.
  - [33] M. Kass, A. Witkin, and D. Terzopoulos, "Snakes: Active contour models," *Int. J. Comput. Vision*, vol. 1, no. 4, pp. 321–331, 1987.
  - [34] D. Terzopoulos, A. Witkin, and M. Kass, "Constraints on deformable models: Recovering 3D shape and nonrigid motion," *Artif. Intell.*, vol. 36, no. 1, pp. 91–123, 1988.
  - [35] W. Wesselink, "Variational modeling of curves and surfaces," Ph.D. dissertation, Utrecht Univ., 1996.
  - [36] J. J. Koenderink, "The structure of images," *Biol. Cybern.*, vol. 50, pp. 363–370, 1984.
  - [37] L. M. J. Florack, B. M. ter Haar Romeny, J. J. Koenderink, and M. A. Viergever, "Scale and the differential structure of images," *Image Vision Comput.*, vol. 10, no. 6, pp. 376–388, July/Aug. 1992.
  - [38] R. M. Hoogeveen, C. J. G. Bakker, and M. A. Viergever, "Limits to the accuracy of vessel diameter measurement in MR angiography," *J. Magn. Reson. Imag.*, vol. 8, pp. 1228–35, 1998.
  - [39] R. M. Hoogeveen, C. J. G. Bakker, and M. A. Viergever, "MR phase-contrast flow measurement with limited spatial resolution in small vessels: Value of model-based image analysis," *Magn. Res. Med.*, vol. 41, no. 3, pp. 520–528, Mar. 1999.
  - [40] L. Piegl and W. Tiller, *The NURBS Book* (Monographs in Visual Communication), 2nd ed. Berlin, Germany: Springer-Verlag, 1996.
  - [41] Y. P. Du, D. L. Parker, W. L. Davis, and G. C. Cao, "Reduction of partial volume artifacts with zero-filled interpolation in three-dimensional MR angiography," *J. Magn. Reson. Imag.*, vol. 4, no. 5, pp. 733–741, 1994.
  - [42] E. H. W. Meijering, K. J. Zuiderveld, and M. A. Viergever, "Image reconstruction by convolution with symmetrical piecewise  $n$ th order polynomial kernels," *IEEE Trans Image Processing*, vol. 8, pp. 192–201, Feb. 1999.
  - [43] W. E. Lorensen and H. E. Cline, "Maring cubes: A high resolution 3D surface reconstruction algorithm," in *Computer Graphics: SIGGRAPH'87 Conf. Proc.*, July 1987, vol. 21, pp. 163–169.
  - [44] W. H. Press, S. A. Teukolsky, W. T. Vetterling, and B. P. Flannery, *Numerical Recipes in C: The Art of Scientific Computing*, 2nd ed. Cambridge, U.K.: Cambridge Univ. Press, 1992.
  - [45] R. F. Smith, B. K. Rutt, A. J. Fox, R. N. Rankin, and D. W. Holdsworth, "Geometric characterization of stenosed human carotid arteries," *Acad. Radiol.*, vol. 3, pp. 898–911, 1996.
  - [46] D. D. Blatter, A. L. Bahr, D. L. Parker, R. O. Robison, J. A. Kimball, D. M. Perry, and S. Horn, "Cervical carotid MR angiography with multiple overlapping thin-slab acquisition: Comparison with conventional angiography," *Amer. J. Roentgenol.*, vol. 161, no. 6, pp. 1269–77, Dec. 1993.
  - [47] Y. Sato, T. Araki, M. Hanayama, H. Naito, and S. Tamura, "A viewpoint determination system for stenosis diagnosis and quantification in coronary angiographic image acquisition," *IEEE Trans. Med. Imag.*, vol. 17, pp. 121–137, Feb. 1998.